

A HIGH-RESOLUTION FINITE VOLUME SEISMIC MODEL TO GENERATE SEAFLOOR DEFORMATION FOR TSUNAMI MODELING

CHRISTOPHER J. VOGL* AND RANDALL J. LEVEQUE†

Abstract. A high-resolution finite volume method approach to incorporating time-dependent slip across rectangular subfaults when modeling general fault geometry is presented. The fault slip is induced by a modification of the Riemann problem to the linear elasticity equations across cell interfaces aligned with the subfaults. This is illustrated in the context of the high-resolution wave-propagation algorithms that are implemented in the open source Clawpack software (www.clawpack.org), but this approach could be easily incorporated into other Riemann solver based numerical methods. Surface deformation results are obtained in both two and three dimensions and compared to those given by the steady-state, homogeneous half-space Okada solution.

Key words. Clawpack, GeoClaw, fault slip, Riemann problem, Okada, tsunami source, subduction zone, embedded interface

1. Introduction. Tsunamigenic megathrust earthquakes generally occur in subduction zones, where an oceanic plate is subducting beneath a continental plate. Stress can build up in locked regions and be violently released. The resulting seafloor motion causes a disturbance of the sea surface that gives rise to gravity waves in the fluid layer. For recent events, it is often the slip on the fault surface that is estimated via inversion techniques from seismic or other observations [5, 6, 16]. In order to perform tsunami simulation, it is necessary to transform this fault slip into seafloor deformation. To do this, the earth is typically modeled as a homogeneous, isotropic half-space, where a Green’s function solution exists for steady-state linear elasticity with a delta function displacement at a point in the interior. Often the fault surface is approximated by a collection of planar subfaults, e.g. rectangular patches on which the slip is assumed to be constant. Integrating the Green’s function over a rectangular subfault gives an explicit expression for the surface deformation as a function of the parameters defining the subfault geometry and the slip. By linearity, these can be summed over the subfaults in order to approximate the deformation from a more complex source [20]. In the tsunami modeling literature, this is often called the Okada solution, using the explicit formulas derived by Okada [18] for rectangular patches.

This solution, however, only approximates the final static deformation of the surface and does not approximate the transient motion that occurs as seismic waves propagate during the earthquake. It also assumes the surface is flat, while in practice the seafloor is not flat. In particular, the region of maximum surface displacement for subduction zone earthquakes is typically near the relatively steep continental slope at the edge of the shelf, which often terminates in a trench that is deeper than the ocean farther offshore. In tsunami modeling, the Okada solution on the flat surface is typically transferred directly to the actual topography. It is also often assumed that the water column above each point on the seafloor is instantaneously lifted by the sea floor deformation [17], causing a displacement of the initially flat sea surface that exactly matches the Okada solution. In this case, one can think of the Okada model as incorporating the ocean into the elastic half space, ignoring the jump in material properties that occurs at the seafloor/water interface.

*Department of Applied Mathematics, University of Washington, Seattle, WA chris.j.vogl@gmail.com.

†Department of Applied Mathematics, University of Washington, Seattle, WA rjl@uw.edu.

Moreover, it is often assumed that the steady state static deformation occurs instantaneously during the earthquake, when in reality the rupture may grow and propagate over the course of several minutes. This can be modeled to some extent using the Okada model by allowing subfaults to rupture at different times and by assuming the resulting static deformation grows over some “rise time” associated with the subfault. This quasi-static approach is often used in tsunami modeling, particularly for events such as the 2004 Sumatra-Andaman earthquake that gave rise to the devastating Indian Ocean tsunami. This 1200km long fault ruptured over the course of about 10 minutes. The quasi-static Okada approach is considered generally adequate for many modeling problems, taking into account the uncertainty in the input variables (slip, rupture time, rise time) that are often poorly constrained from observations and inversions, even for recent event. This approach is implemented in the GeoClaw software that is widely used for tsunami modeling [1, 12], as well as by Dutykh et al. [4].

For some problems, however, more accurate estimates of sea surface displacement may be required, and in some cases even the transient seismic waves in the earth and associated acoustic waves in the ocean may be important to model. For example, Dutykh and Dias [3] noted that transient effects can cause a leading depression wave where an elevation wave is expected. An important potential application is to the study of early warning systems that might be used to provide enhanced warnings based on observations obtained in the source region during and immediately following a major earthquake [17]. Recent work by Kozdon and Dunham [7], by Maeda, Furumuro, and collaborators [13, 14], and by Saito and Tsushima [19], for example, has shown that the study of coupled seismic and acoustic waves could be useful in rapid inversion to distinguish between different rupture models. Our work is a part of an ongoing study of the feasibility and potential uses of a cabled network of sea floor sensors to monitor the Cascadia Subduction Zone [22]. Thus, the goal herein is to develop a high-resolution finite volume method for solving the seismic wave equations (eventually to be coupled with the ocean) that allows the specification of arbitrary slip on a fault surface and works well in the context of the open source Clawpack software [2, 15], which includes adaptive mesh refinement (AMR) algorithms in both two and three space dimensions. In addition to providing an efficient and accurate solver for these equations, this will facilitate coupling with the GeoClaw software that is also built on the Clawpack AMR framework and distributed as part of that software.

This paper focuses on the homogeneous half-space problem in order to verify that the method and implementation presented here can reproduce the exact Okada solution. After deriving the modified Riemann solutions in Sect. 2, computed surface deformations are obtained for a two-dimensional vertical cross section and for a full three-dimensional problem in Sect. 3. Concluding remarks and discussion of ongoing extensions of this work, including the addition of an ocean layer and seafloor topography, are found in Sect. 4. The code producing the simulations shown in this paper is archived at [21] and active development work can be followed in the Github repository at github.com/clawpack/seismic.

2. The elasticity Riemann solver with fault slip. The equations of isotropic linear elasticity can be written as

$$(1) \quad \begin{aligned} \sigma_t - \lambda(\nabla \cdot u)I - \mu(\nabla u + \nabla^T u) &= 0, \\ \rho u_t - \nabla \cdot \sigma &= 0, \end{aligned}$$

where σ is the symmetric stress tensor, u is the velocity, I is the identity tensor, ρ is the density, and λ, μ are the Lamé parameters. The wave-propagation algorithm discussed in [11] uses the solutions to the Riemann problems at grid cell interfaces to update cell quantities. This approach extends to other materials, such as orthotropic and poroelastic materials [8, 9, 10]. Here, the fault slip is introduced by modifying the Riemann problems, and corresponding solutions, at cell interfaces that line up with the fault. Given that two-dimensional simulations can be performed in much less time than in three dimensions, the plane-strain case is used first for comparing against the Okada solution for various faults of infinite length in the strike direction. The slip model is also extended to three dimensions and compared to the corresponding Okada solution for a fault of finite length.

2.1. Two dimensions (plane-strain). In the two-dimensional, plane-strain case, the equations take the form

$$(2) \quad \begin{aligned} \sigma_t^{11} - (\lambda + 2\mu)u_x^1 - \lambda u_y^2 &= 0, \\ \sigma_t^{22} - \lambda u_x^1 - (\lambda + 2\mu)u_y^2 &= 0, \\ \sigma_t^{12} - \mu(u_x^2 + u_y^1) &= 0, \\ \rho u_t^1 - \sigma_x^{11} - \sigma_y^{12} &= 0, \\ \rho u_t^2 - \sigma_x^{12} - \sigma_y^{22} &= 0, \end{aligned}$$

where superscripts denote components in the x (horizontal) and y (vertical) directions, respectively. This models a vertical slice of the earth ($y \leq 0$) with an infinitely long fault in the orthogonal direction. In heterogeneous media, the density ρ and the Lamé parameters λ, μ can be spatially varying, which results in the following linear hyperbolic system of equations in non-conservative form:

$$q_t + A(x, y)q_x + B(x, y)q_y = 0,$$

where $q = [\sigma^{11}, \sigma^{22}, \sigma^{12}, u^1, u^2]^T$ and A and B are the 5×5 coefficient matrices. As shown in [11], the general Riemann solution involves the eigenvectors of $n_x A + n_y B$, where $n = [n_x, n_y]^T$ is the normal vector to the cell-edge. These vectors are

$$(3) \quad r_{\pm}^p = \begin{bmatrix} \lambda + 2\mu n_x^2 \\ \lambda + 2\mu n_y^2 \\ 2\mu n_x n_y \\ \mp c_p n_x \\ \mp c_p n_y \end{bmatrix} \quad \text{and} \quad r_{\pm}^s = \begin{bmatrix} -2\mu n_x n_y \\ 2\mu n_x n_y \\ \mu(n_x^2 - n_y^2) \\ \pm c_s n_y \\ \mp c_s n_x \end{bmatrix},$$

where r_{\pm}^p and r_{\pm}^s correspond to the P- and S- waves traveling either in the direction of the normal (+) or opposite (-).

Denote q_{\pm}^* and q_{\pm} as the initial and resulting states, respectively, on corresponding sides of the cell-edge. These are related via

$$\begin{aligned} q_+ &= q_+^* - \alpha_+^p r_+^p - \alpha_+^s r_+^s, \\ q_- &= q_-^* + \alpha_-^p r_-^p + \alpha_-^s r_-^s. \end{aligned}$$

where the α 's are amplitudes of the P-waves and S-waves. To couple q_+ with q_- , continuity of normal traction ($\sigma_n := \sigma \cdot n \cdot n$) and normal velocity ($u_n := u \cdot n$) are enforced across the cell-edge. The fault slip is now implemented by enforcing a slip

rate s evenly to the two tangential velocities (u_τ) on either side of the cell-edge. These conditions are summarized in matrix form:

$$\begin{aligned} P_n q_- &= P_n q_+, \quad P_\tau q_- = s/2, \quad \text{and} \quad P_\tau q_+ = -s/2, \\ \text{where } P_n q &:= \begin{bmatrix} n_x^2 & n_y^2 & 2n_x n_y & 0 & 0 \\ 0 & 0 & 0 & n_x & n_y \end{bmatrix} q = \begin{bmatrix} \sigma_n \\ u_n \end{bmatrix} \\ \text{and } P_\tau q &:= \begin{bmatrix} 0 & 0 & 0 & n_y & -n_x \end{bmatrix} q = \begin{bmatrix} u_\tau \end{bmatrix}. \end{aligned}$$

The resulting states q_\pm are exchanged for the initial states and eigenvectors to obtain equations for α_\pm^p and α_\pm^s . Noting that $P_n r_\pm^s = 0$ and $P_\tau r_\pm^p = 0$ helps to greatly simplify the system:

$$\begin{aligned} \begin{bmatrix} P_n r_+^p & P_n r_-^p & 0 & 0 \end{bmatrix} \begin{bmatrix} \alpha_+^p \\ \alpha_-^p \end{bmatrix} &= P_n (q_+^* - q_-^*), \\ \begin{bmatrix} P_\tau r_+^s & 0 \\ 0 & P_\tau r_-^s \end{bmatrix} \begin{bmatrix} \alpha_+^s \\ \alpha_-^s \end{bmatrix} &= \begin{bmatrix} P_\tau q_+^* + s/2 \\ -P_\tau q_-^* + s/2 \end{bmatrix}. \end{aligned}$$

The solution is

$$(4) \quad \alpha_\pm^p = \frac{c_{p\mp} \Delta \sigma_n^* \mp B_\mp \Delta u_n^*}{c_{p+} B_- + c_{p-} B_+} \quad \text{and} \quad \alpha_\pm^s = \frac{u_{\tau\pm}^* \pm s/2}{c_{s\pm}},$$

where $\Delta \sigma_n^* := \sigma_{n+}^* - \sigma_{n-}^*$ and $\Delta u_n^* := u_{n+}^* - u_{n-}^*$.

At cell-edges that correspond to a subfault, the goal is to obtain a total displacement S over a time period Δt , beginning at some rupture time t_r . Thus, for time $t_r \leq t \leq t_r + \Delta t$, the slip rate is imposed as $s = S/\Delta t$ (uniform slip in time). The variable time-stepping algorithm in Clawpack is adjusted so that Δt is divided into an integer number of time steps. When the slip rate is zero, the standard Riemann solution is used where continuity of traction and velocity are enforced across the cell-edge.

2.2. Additional numerical details. Fig. 1 shows a few time frames of a simulation in which unit slip is imposed for $0 \leq t \leq 1$ across a fault with dip angle of 0.2 radians (≈ 11.5 degrees), top-edge depth 100km, and fault plane width 50km. The AMR capability of Clawpack is utilized with 8 cells spanning the fault at the coarsest grid level and a Courant number set to 0.9. There are then 5 additional levels of grids, each twice as refined as the previous level in both space and time. Note that as the seismic waves propagate out, a static stress field remains near the fault plane that indicates a permanent deformation of equal magnitude, but opposite sign, on either side of the fault. For this figure, the fault is deep beneath the surface and so the waves continue propagating outward. In reality, the depth of the fault may be quite shallow relative to its width, so the upward propagating waves would reflect off the surface ($y = 0$) by the time shown in this figure.

To address this, a free-surface boundary condition is imposed at the surface by setting ghost cell values in such a way that there is zero traction at the free surface. More specifically, for $h > 0$, the value of $\sigma^{i2}(x, h)$ is set to $-\sigma^{i2}(x, -h)$, so that $\sigma^{i2}(x, 0) \approx (1/2)[\sigma^{i2}(x, h) + \sigma^{i2}(x, -h)] = 0$ for $i = 1, 2$. A mapped grid, $(X, Y) = \mathcal{M}(x, y)$, is used that lines up with both the fault and the free surface. This is accomplished by interpolating between a normal Cartesian grid ($\mathcal{M}^s(x, y) = (x, y)$) and a grid that is rotated to line up with the fault: $\mathcal{M}^f(x, y) = (x_c + \cos(\theta)(x - x_c) + \sin(\theta)(y - y_c), y_c - \sin(\theta)(x - x_c) + \cos(\theta)(y - y_c))$, where (x_c, y_c) is the centroid of

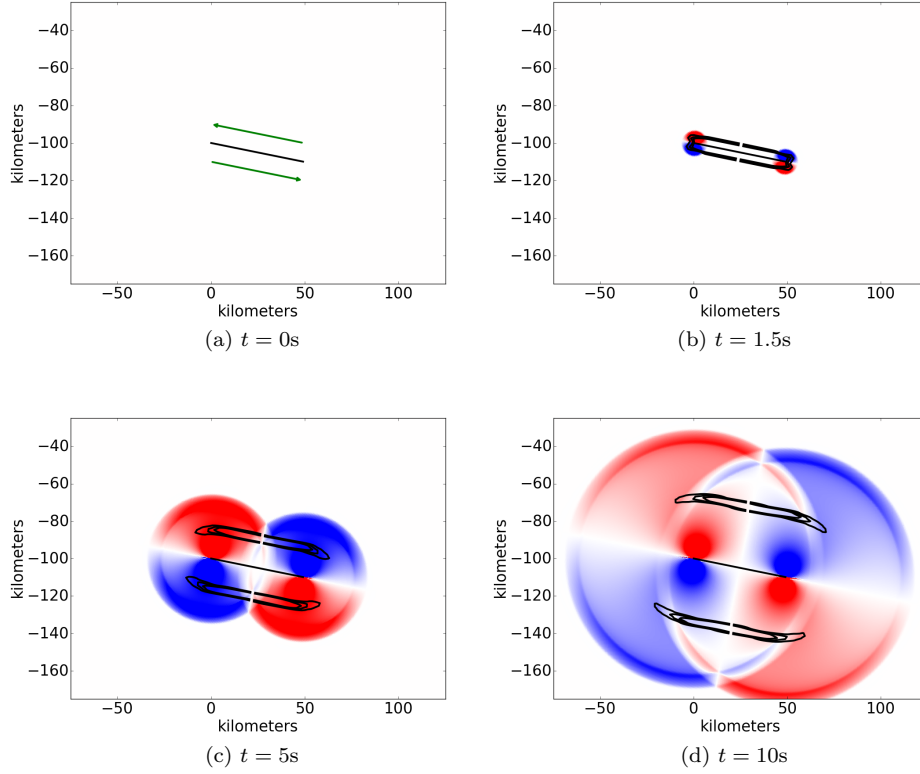


Fig. 1: Compression/tension and shear waves emanating from a 1km, 1s uniform slip across a fault with dip 0.2rad, top-edge depth 100km, and width 50km, shown at four different times (red: compression, blue: tension, black lines: contours of velocity in the direction tangent to the fault).

the fault and θ the dip angle. A distance from the fault is defined as

$$\phi(x, y) = \begin{cases} \sqrt{(x - x_l)^2 + (y - y_c)^2} & \text{for } x < x_l \\ |y - y_c| & \text{for } x_l \leq x \leq x_r \\ \sqrt{(x - x_r)^2 + (y - y_c)^2} & \text{for } x_r < x \end{cases},$$

where $x_l = x_c - W/2$ and $x_r = x_c + W/2$ for fault width W . The grid mapping is now complete as $\mathcal{M}(x, y) = \mathcal{M}^s(x, y)\phi(x, y)/y_c + \mathcal{M}^f(x, y)(1 - \phi(x, y)/y_c)$, for $\phi(x, y) \leq y_c$, and $\mathcal{M}(x, y) = \mathcal{M}^s(x, y)$ otherwise. A visualization of this mapped grid is found in Fig. 2.

2.3. Extension to three dimensions. Consider the three-dimensional elasticity equation (1) written in non-conservative form:

$$q_t + A(x, y, z)q_x + B(x, y, z)q_y + C(x, y, z)q_z = 0,$$

$$q = [\sigma^{11}, \sigma^{22}, \sigma^{33}, \sigma^{12}, \sigma^{23}, \sigma^{13}, u^1, u^2, u^3]^T,$$

where positive x is east, positive y is north, and positive z is up. A similar modification to the Riemann problem for this equation is made to incorporate fault slip.

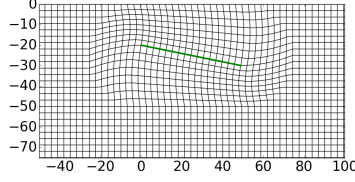


Fig. 2: Mapped grid conforming both to fault and to surface.

In order to simplify the extension to three dimensions, only faults with strike angle of 0 degrees (top edge pointing north) and rake angle of 90 degrees (slip is in dip direction) are considered. Note these types of faults are the most common in subduction zones. The mapped grid is an extension of the two-dimensional mapping near the fault: $\mathcal{M}(x, y, z) = \mathcal{M}^s(x, y, z)\phi(x, z)/z_c + \mathcal{M}^f(x, y, z)(1 - \phi(x, z)/z_c)$. Note that this mapping is invariant to y , and thus the general Riemann solutions either involve the eigenvectors to $n_x A + n_z C$ or to B , because the normal to the cell-faces is either $n = [n_x, 0, n_z]^T$ or $n = [0, 1, 0]^T$.

If $n = [0, 1, 0]^T$, the standard Riemann solution for (1) is used because no slip is to be imposed. Thus, assume $n = [n_x, 0, n_z]^T$. Denote the tangent vectors $\tau_1 = [n_z, 0, -n_x]^T$ and $\tau_2 = [0, 1, 0]^T$, noting that τ_1 points in the rake direction and τ_2 is orthogonal to τ_1 . The eigenvectors of $n_x A + n_z C$ are

$$(5) \quad r_{\pm}^p = \begin{bmatrix} \lambda + 2\mu n_x^2 \\ \lambda \\ \lambda + 2\mu n_z^2 \\ 0 \\ 0 \\ 2\mu n_x n_z \\ \mp c_p n_x \\ 0 \\ \mp c_p n_z \end{bmatrix}, \quad r_{\pm}^{s1} = \begin{bmatrix} -2\mu n_x n_z \\ 0 \\ 2\mu n_x n_z \\ 0 \\ 0 \\ \mu(n_z^2 - n_x^2) \\ \pm c_s n_z \\ 0 \\ \mp c_s n_x \end{bmatrix}, \quad \text{and } r_{\pm}^{s2} = \begin{bmatrix} 0 \\ 0 \\ 0 \\ \mu n_x \\ \mu n_z \\ 0 \\ \mp c_s \\ 0 \end{bmatrix}.$$

The initial and resulting states are again related via these eigenvectors: $q_{\pm} = q_{\pm}^* \mp \alpha_{\pm}^p r_{\pm}^p \mp \alpha_{\pm}^{s1} r_{\pm}^{s1} \mp \alpha_{\pm}^{s2} r_{\pm}^{s2}$. The conditions at the cell-face are now continuity of normal traction ($\sigma \cdot n$) and normal velocity ($u \cdot n$), an evenly imposed slip rate s in the two τ_1 velocities, and zero velocity in the τ_2 direction. As before, these conditions are summarized in matrix form:

$$P_n q_- = P_n q_+, \quad P_{\tau_1} q_- = s/2, \quad P_{\tau_1} q_+ = -s/2, \quad \text{and } P_{\tau_2} q_{\pm} = 0,$$

where $P_n q := \begin{bmatrix} n_x^2 & 0 & n_z^2 & 0 & 0 & 2n_x n_z & 0 & 0 & 0 \\ 0 & 0 & 0 & 0 & 0 & 0 & n_x & 0 & n_z \end{bmatrix} q = \begin{bmatrix} \sigma_n \\ u_n \end{bmatrix}$,

$$P_{\tau_1} q := \begin{bmatrix} 0 & 0 & 0 & 0 & 0 & 0 & n_z & 0 & -n_x \end{bmatrix} q = \begin{bmatrix} u_{\tau_1} \end{bmatrix},$$

and $P_{\tau_2} q := \begin{bmatrix} 0 & 0 & 0 & 0 & 0 & 0 & 0 & 1 & 0 \end{bmatrix} q = \begin{bmatrix} u_{\tau_2} \end{bmatrix}$.

The resulting states are again exchanged for the initial states and eigenvectors, and again it is useful to note that $P_n r_{\pm}^{s1} = P_n r_{\pm}^{s2} = 0$, $P_{\tau_1} r_{\pm}^p = P_{\tau_1} r_{\pm}^{s2} = 0$, and $P_{\tau_2} r_{\pm}^p = P_{\tau_2} r_{\pm}^{s1} = 0$. The solution to the resulting system is

$$(6) \quad \alpha_{\pm}^p = \frac{c_{p\mp} \Delta \sigma_n^* \mp B_{\mp} \Delta u_n^*}{c_{p+} B_- + c_{p-} B_+}, \quad \alpha_{\pm}^{s1} = \frac{u_{\tau_1}^* \pm s/2}{c_{s\pm}}, \quad \text{and } \alpha_{\pm}^{s2} = 0.$$

3. Comparison of Numerical Results with the Okada Solution. In Sect. 2.1, fault slip is modeled in a plane-strain, linearly elastic solid (2) by modifying the corresponding Riemann problems (3)-(4) in a novel way. This approach is then extended to three dimensions (1) and the modified Riemann solutions (5)-(6) given. To verify this approach, the Okada solution is used as implemented in the GeoClaw ‘dtopotools’ Python module¹. Surface deformation is computed by numerically integrating the velocity at fixed gauge locations along the surface. These values are then compared to those of the Okada solution at the same spatial locations.

3.1. Numerical results in two dimensions. For the plane-strain case, a baseline fault is chosen with unit slip for $0 \leq t \leq 1$, dip 0.2 radians (≈ 11.5 degrees), top-edge depth 20km, and fault plane width 50km. Fig. 3 shows the resulting simulation at various times. Note that the seismic waves interact with the free surface at the top of the domain, both reflecting off of and traveling along the surface, leaving behind a static deformation. As the waves propagate away, the surface deformation approaches that of the Okada solution. At $t = 90$ s, with the same AMR strategy used for the results in Fig. 1, the numerical solution was shown to converge to the Okada solution as the number of cells across the fault at the coarsest level is increased. With 8 cells, the difference between the numerical results at $t = 90$ s and the Okada solution is less than 2% relative to the maximum Okada deformation.

To ensure the robustness of this approach to physical fault parameters, the baseline fault is modified to obtain three additional faults. Fig. 4 shows the results for a fault with greater top-edge depth (40km vs 20km), another with a greater dip angle (≈ 22.9 degrees vs ≈ 11.5 degrees), and a third with shorter width (25km vs 50km). Note that all fault geometries studied show very close agreement, both in vertical and horizontal displacement, with the corresponding Okada solutions. As an additional test, the fault slip profile is also varied. Let W denote the fault width, $p \in [0, W]$ denote the down-dip distance from the top of the fault, $p_0 = W/2$, $p_1 = W/4$, and $p_2 = 3W/4$. A smooth fault profile of $S(p) = [1 + \cos(\pi(p - p_0)/p_0)]/2$ is chosen, along with a bi-modal profile $S(p) = [1 + \cos(\pi(p - p_1)/p_1)]/2$ for $p \in [0, p_0]$ and $S(p) = [1 + \cos(\pi(p - p_2)/p_1)]/2$ for $p \in (p_0, W]$. The results, also in Fig. 4, show good agreement with the corresponding Okada solutions in all cases.

3.2. Numerical results in three dimensions. Next, the extension to three space dimensions from Sect. 2.3 is verified. Similar to what was done in the two-dimensional simulations, a three-dimensional fault is chosen with unit slip for $0 \leq t \leq 1$, strike 0 degrees, rake 90 degrees, dip 0.2 radians (≈ 11.5), centroid depth 25km, 50km of width in the dip direction, and 25km of length in the strike direction. The AMR strategy uses 8 cells across the dip direction and 4 cells across the strike direction at the coarsest level, with 3 additional levels of refinement. In two dimensions, the corresponding resolution gave a relative error of less than 4%. Fig. 5 shows the seismic waves again interacting with the free surface at the top of the domain. Again, this interaction causes deformation in the surface that, after the waves propagate out of the domain, approaches the Okada solution. At $t = 70$, the agreement between the numerical and Okada solution is very good.

¹See www.clawpack.org/okada.html

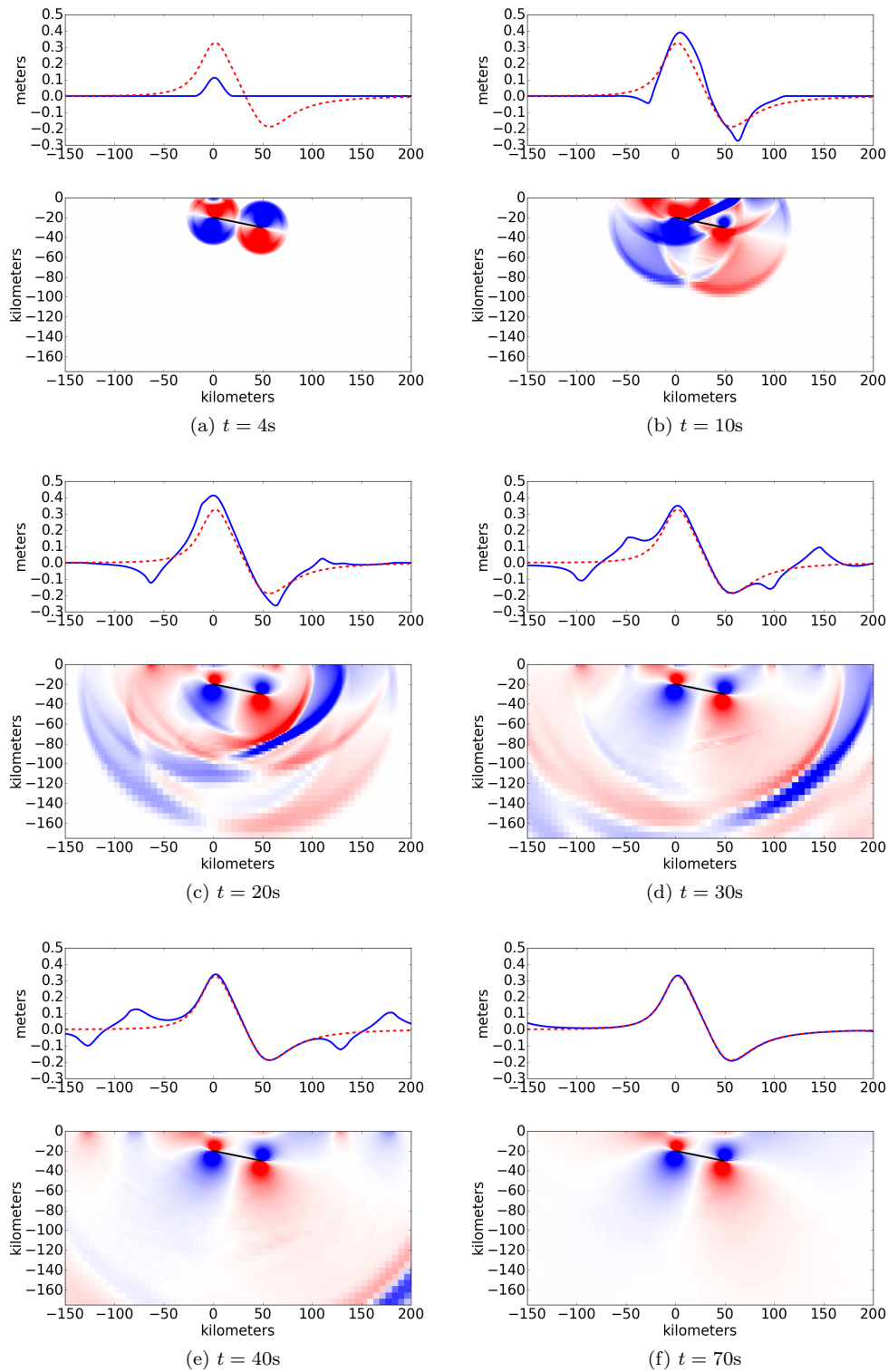


Fig. 3: Results for a 1km, 1s uniform slip across a fault with dip 0.2rad, top-edge depth 20km, and width 50km. The upper plot at each time shows the surface deformation (blue solid line - numerical surface displacement, red dashed line - Okada solution), and the lower plot shows the compression/tension waves (red: compression, blue: tension).

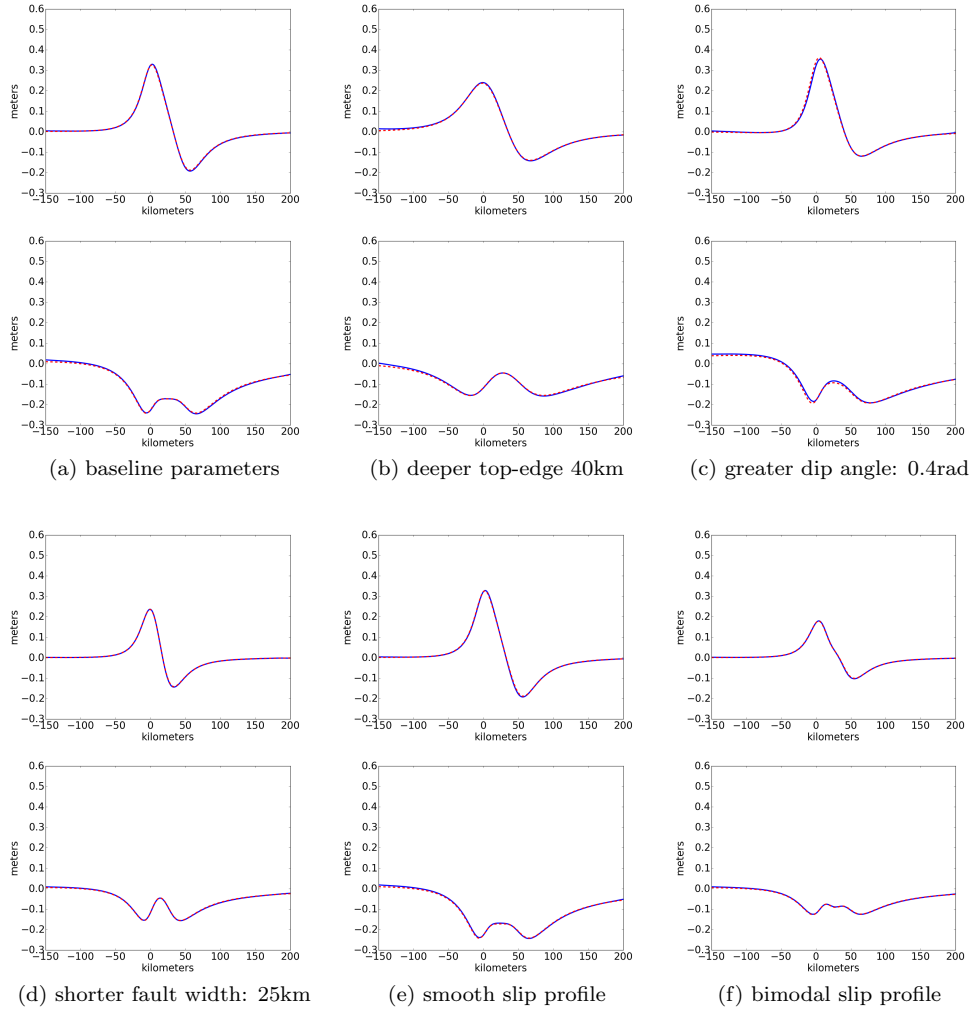


Fig. 4: Vertical (top) and horizontal (bottom) surface displacement at $t = 90s$ matching that of Okada for fault parameters varying from the baseline of a 1km, 1s uniform slip across a fault with dip 0.2rad, top-edge depth 100km, and width 50km (Blue solid line: numerical solution, red dashed line: Okada solution).

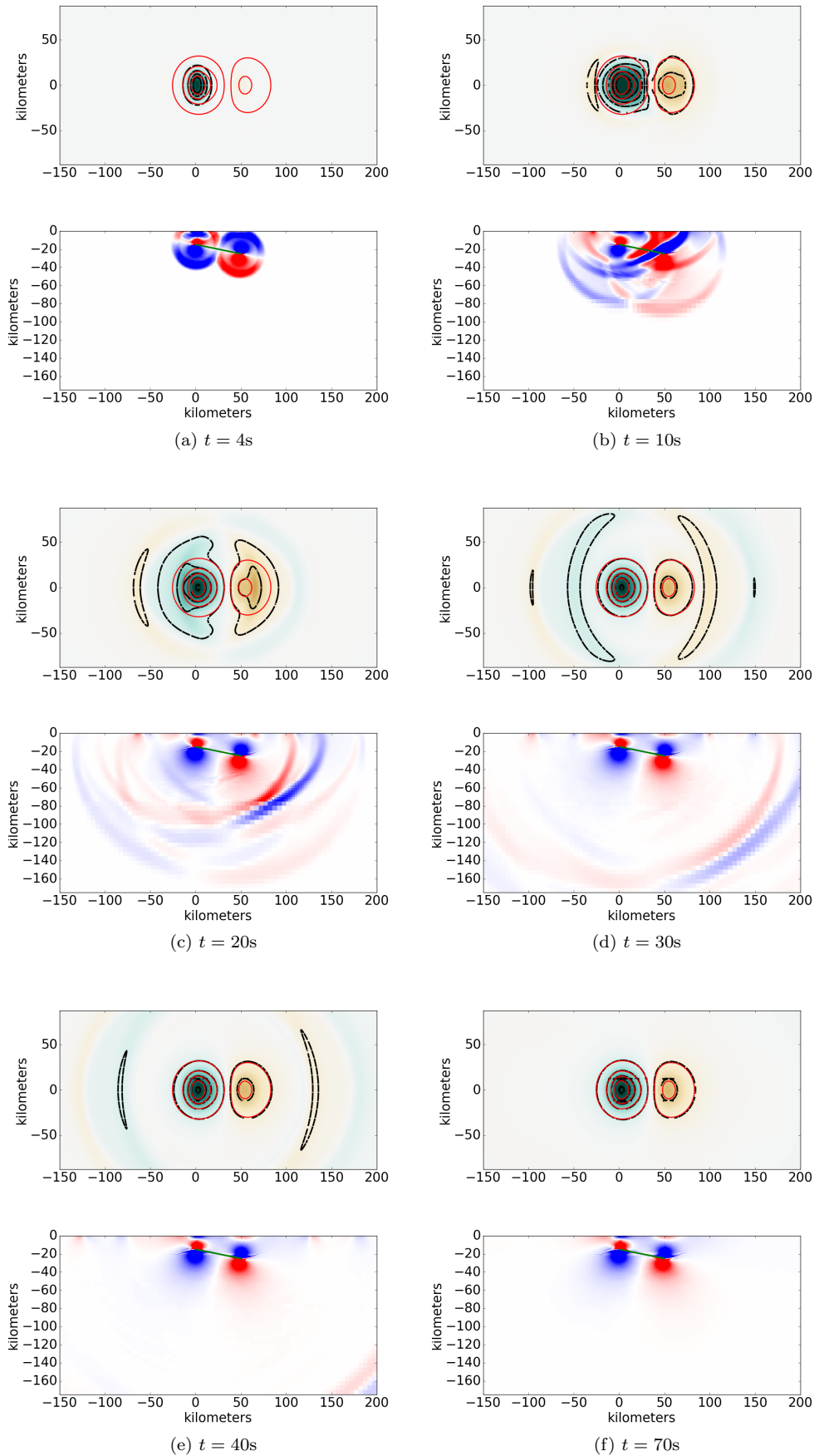


Fig. 5: The upper plot at each time shows a plane view of the surface deformation

4. Conclusion and Discussion. While the Okada solution is often adequate for tsunami simulation, the Okada assumptions of instantaneous displacement in a homogeneous half-space may be inadequate for some applications. This work presents a novel way to introduce fault slip via the Riemann problems in the Clawpack simulation software to fully model the seismic waves and transient motion of the seafloor. When solving the linear elasticity hyperbolic system, both in three dimensions (1) and in the case of plane-strain (2), the Riemann solution at a cell interface imposes the slip velocity in the dip direction instead of imposing continuity of tangential traction and velocity. The corresponding eigenvectors (3),(5) and coefficients (4),(6) are then used by the high-resolution wave-propagation algorithm implemented in Clawpack to solve for surface deformation.

Two-dimensional results from a baseline fault initially differ from that of Okada for small t but then evolve towards the steady-state solution for larger t , as is expected. Physical parameters are varied to observe results for deeper faults, steeper faults, faults of various width, and faults with spatially varying slip profiles. All the dynamic simulations show agreement with the corresponding Okada solution once the seismic waves propagate sufficiently away from the region of interest. The approach is extended to three dimensions and applied to a dipping fault. Again, the dynamic solution evolves towards the corresponding Okada solution.

The Riemann solution presented here does not assume the elastic medium is homogeneous. Thus, current work involves including an ocean layer as a second elastic medium with a zero shear modulus. This permits direct observation of the sea surface deformation instead of relying on the assumption that the sea surface moves instantaneously with the seafloor. Other current work involves incorporating varying topography, which can also be implemented via the mapped grid approach presented here. Potential future work may include the varying densities of the subduction zone plates and a gravitational force. Finally, it should be noted that this approach to modifying the Riemann problems can be generalized to include a variety of conditions on an interface embedded in an elastic solid, including jumps in tangential or normal traction.

acknowledgements. The authors are grateful to Grady Lemoine for discussions of this work, in particular those involving the modification of the Riemann problems to incorporate fault slip.

REFERENCES

- [1] M. J. BERGER, D. L. GEORGE, R. J. LEVEQUE, AND K. T. MANDLI, *The GeoClaw software for depth-averaged flows with adaptive refinement*, Adv. Water Res., 34 (2011), pp. 1195–1206.
- [2] CLAWPACK DEVELOPMENT TEAM, *Clawpack software*, (2014), doi:10.5281/zenodo.50982. Version 5.3.1.
- [3] DENYS DUTYKH AND FRÉDÉRIC DIAS, *Tsunami generation by dynamic displacement of sea bed due to dip-slip faulting*, Mathematics and Computers in Simulation, 80 (2009), pp. 837–848, doi:10.1016/j.matcom.2009.08.036.
- [4] DENYS DUTYKH, DIMITRIOS MITSOTAKIS, XAVIER GARDEIL, AND FRÉDÉRIC DIAS, *On the use of the finite fault solution for tsunami generation problems*, Theoretical and Computational Fluid Dynamics; Heidelberg, 27 (2013), pp. 177–199, doi:http://dx.doi.org/10.1007/s00162-011-0252-8.
- [5] STEPHEN HARTZELL, PENGCHENG LIU, AND CARLOS MENDOZA, *The 1994 Northridge, California, earthquake: Investigation of rupture velocity, risetime, and high-frequency radiation*, J. Geophys. Res., 101 (1996), pp. 20091–20108, doi:10.1029/96JB01883.
- [6] CHEN JI, DAVID J. WALD, AND DONALD V. HELMBERGER, *Source Description of the 1999 Hector Mine, California, Earthquake, Part I: Wavelet Domain Inversion Theory and Resolu-*

- tion Analysis*, Bulletin of the Seismological Society of America, 92 (2002), pp. 1192–1207, doi:10.1785/0120000916.
- [7] J. E. KOZDON AND E. M. DUNHAM, *Constraining shallow slip and tsunami excitation in megathrust ruptures using seismic and ocean acoustic waves recorded on ocean-bottom sensor networks*, Earth and Planetary Science Letters, 396 (2014), pp. 56–65, doi:10.1016/j.epsl.2014.04.001.
- [8] G. I. LEMOINE, *Three-Dimensional Mapped-Grid Finite Volume Modeling of Poroelastic-Fluid Wave Propagation*, SIAM J. Sci. Comput., 38 (2016), pp. B808–836, doi:10.1137/130934866.
- [9] G. I. LEMOINE AND M.-Y. OU, *Finite Volume Modeling of Poroelastic-Fluid Wave Propagation with Mapped Grids*, SIAM J. Sci. Comput., 36 (2014), pp. B396–B426, doi:10.1137/130920824.
- [10] G. I. LEMOINE, M.-Y. OU, AND R. J. LEVEQUE, *High-resolution finite volume modeling of wave propagation in orthotropic poroelastic media*, SIAM J. Sci. Comput., 35 (2013), pp. B176–B206, doi:10.1137/120878720.
- [11] R. J. LEVEQUE, *Finite Volume Methods for Hyperbolic Problems*, Cambridge University Press, 2002.
- [12] R. J. LEVEQUE, D. L. GEORGE, AND M. J. BERGER, *Tsunami modeling with adaptively refined finite volume methods*, Acta Numerica, (2011), pp. 211–289.
- [13] T. MAEDA AND T. FURUMURA, *FDM Simulation of Seismic Waves, Ocean Acoustic Waves, and Tsunamis Based on Tsunami-Coupled Equations of Motion*, Pure Appl. Geophys., 170 (2011), pp. 109–127, doi:10.1007/s00024-011-0430-z.
- [14] T. MAEDA, T. FURUMURA, S. NOGUCHI, S. TAKEMURA, S. SAKAI, M. SHINOHARA, K. IWAI, AND S.-J. LEE, *Seismic- and Tsunami-Wave Propagation of the 2011 Off the Pacific Coast of Tohoku Earthquake as Inferred from the Tsunami-Coupled Finite-Difference Simulation*, Bull. Seis. Soc. Amer., 103 (2013), pp. 1456–1472, doi:10.1785/0120120118.
- [15] KYLE T MANDLI, ARON J AHMADIA, MARSHA BERGER, DONNA CALHOUN, DAVID L GEORGE, YIANNIS HADJIMICHAEL, DAVID I KETCHESON, GRADY I LEMOINE, AND RANDALL J LEVEQUE, *ClauPack: Building an open source ecosystem for solving hyperbolic PDEs*, PeerJ Computer Science, 2 (2016), p. e68, doi:10.7717/peerj-cs.68.
- [16] D. MELGAR AND Y. BOCK, *Kinematic earthquake source inversion and tsunami runup prediction with regional geophysical data*, J. Geophys. Res. Solid Earth, 120 (2015), p. 2014JB011832, doi:10.1002/2014JB011832.
- [17] M. A. NOSOV, *Tsunami waves of seismic origin: The modern state of knowledge*, Izvestiya. Atmospheric and Oceanic Physics; Washington, 50 (2014), pp. 474–484, doi:http://dx.doi.org/10.1134/S0001433814030098.
- [18] Y OKADA, *Surface deformation due to shear and tensile faults in a half-space*, Bull. Seism. Soc. Am., 75 (1985), pp. 1135–1154.
- [19] TATSUHIKO SAITO AND HIROAKI TSUSHIMA, *Synthesizing ocean bottom pressure records including seismic wave and tsunami contributions: Toward realistic tests of monitoring systems*, Journal of Geophysical Research: Solid Earth, 121 (2016), pp. 8175–8195, doi:10.1002/2016JB013195.
- [20] VASILY V. TITOV, FRANK I. GONZALEZ, E. N. BERNARD, MARIE C. EBLE, HAROLD O. MOFJELD, JEAN C. NEWMAN, AND ANGIE J. VENTURATO, *Real-Time Tsunami Forecasting: Challenges and Solutions*, Nat Hazards, 35 (2005), pp. 35–41, doi:10.1007/s11069-004-2403-3.
- [21] CHRISTOPHER J. VOGL AND RANDALL J. LEVEQUE, *Code archive*, (2017), doi:10.5281/zenodo.569351.
- [22] W. S. D. WILCOCK, D. A. SCHMIDT, J. E. VIDALE, AND OTHERS, *Sustained Offshore Geophysical Monitoring in Cascadia*. Whitepaper, The Subduction Zone Observatory Workshop, Boise, 2016, <http://faculty.washington.edu/rjl/pubs/SZ0workshop2016>.